Exceptional Strength-Ductility Combinations of a CoCrNi-Based Medium-Entropy Alloy via Short/Medium-Time Annealing after Hot-Rolling

Yongan Chen , Dazhao Li * , Zhijie Yan , Shaobin Bai , Ruofei Xie , Jian Sheng , Jian Zhang , Shuai Li , Jinzhong Zhang

Posted Date: 16 August 2024

doi: 10.20944/preprints202408.1207.v1

Keywords: medium-entropy alloy; precipitates; mechanical properties; deformation mechanisms

Article

Exceptional Strength-Ductility Combinations of a CoCrNi-Based Medium-Entropy Alloy via Short/Medium-Time Annealing after Hot-Rolling

Yongan Chen [1,2], Dazhao Li [1,*], Zhijie Yan [1,2], Shaobin Bai [3], Ruofei Xie [1,2], Jian Sheng [1,2], Jian Zhang [4], Shuai Li [4] and Jinzhong Zhang [4]

[1] School of Materials Science and Engineering, North University of China, Taiyuan 030051, Shanxi, PR China; cya894589913@163.com (Y.C.); yanzhijie74@163.com (Z.Y.); xieruofei2623@163.com (R.X.); shengjian032@163.com (J.S.)
[2] Shanxi Key Laboratory of Advanced Metal Materials for Special Environments, Taiyuan 030051, Shanxi, PR China
[3] School of Aerospace Engineering, North University of China, Taiyuan 030051, Shanxi, PR China; sh1989bedu@163.com (S.B.)
[4] Department of operation, Guoneng Huaian Co-generation Co., Ltd., Zhangjiakou 076100, Hebei, PR China; 197077723@qq.com (J.Z.); 1064656280@qq.com (S.L.); 209731196@qq.com (J.Z.)
* Correspondence: dazhaoli@163.com

Abstract: Strong yet ductile alloys have long been desired for industrial applications to enhance structural reliability. This work produced two $(CoCrNi)_{93.5}Al_3Ti_3C_{0.5}$ medium-entropy alloys with exceptional strength-ductility combinations, via short/medium (3 min/30 min)-time annealing after hot-rolling. Three types of intergranular precipitates including MC, $M_{23}C_6$ carbides, and $L1_2$ phase were detected in both the samples. Noticeably, the high density of intragranular $L1_2$ precipitates were only founded in the medium-time annealed sample but not in another one. Upon inspection of deformed substructure, it was revealed that the plane slip is the dominant deformation mechanism of both the alloys. This is related to the lower stacking fault energy, higher lattice friction induced by C solute, and slip plane softening caused by intragranular dense $L1_2$ precipitates. Additionally, we noted that the stacking fault and twinning act as the mediated mechanisms in deformation of the short-time annealed alloy, while only the former in the medium-time annealed one. It is attributed to the higher energy stacking faults and the increased critical twinning stress caused by intragranular dense $L1_2$ precipitates that inhibited the twinning tendency. Our present findings provide not only a guidance for optimizing the mechanical properties of high/medium-entropy alloys, but also a fundamental understanding of deformation mechanisms.

Keywords: medium-entropy alloy; precipitates; mechanical properties; deformation mechanisms

1. Introduction

As a class of advance metal materials, high/medium-entropy alloys (H/MEAs) have been given a great promise for breaking the property bottleneck in conventional alloys [1,2]. Among many studies [3–5], an equiatomic CrCoNi MEA with face-centered cubic (FCC) structure has gradually stood out as one of the most damage tolerant alloys to date. Despite the excellent ductility, it always shown lower yield strength of even about ~350 MPa, because of the multiple slip systems like in other FCC alloys [6]. This severely limits its engineering serviceability for structural applications. Exploring appropriate strategies to overcome the strength-ductility trade-off has been a major objective for the CrCoNi MEA [7].

Many studies [8,9] have shown that the precipitation strengthening by coherent $L1_2$ phase may be an ideal method for enhancing the strength of FCC-structured H/MEAs without excessive expense of ductility. For example, Zhao et al. [10] produced a $L1_2$ phase-strengthened CoCrNi-based MEA by alloying of Al and Ti elements, which exhibited decent yield strength of 750 MPa with excellent

 doi:10.20944/preprints202408.1207.v1

plasticity of 45%. Wang et al. [11] reported a similar $(CoCrNi)_{94}Al_3Ti_3$ MEA, strengthened by $L1_2$ phase, with the yield strength of 900 MPa and fracture strain of 22.9%. In these studies [8–11], the $L1_2$ phase usually coexists in both intergranular and intragranular forms, as a result of discontinuous and continuous precipitations, respectively. It was revealed [10,11] that the intragranular $L1_2$ precipitates with generally high-density and nano-size, can not only hinder dislocation motion to enhance strength, but also allow the dislocations shearing through them to maintain plasticity.

There is another effective strategy to enhance the FCC-H/MEAs by C-doping has also been widely reported [12,13]. In general, the interstitial C element plays a dual role in producing solid solution strengthening and introducing the carbides to trigger precipitation strengthening. Wang et al. [14] revealed in an FCC-HEA that the yield strength is linearly related to the C content with a specific growth rate of 184 MPa/at.%. Evidently, the effectiveness produced by solid solution strengthening is relatively limited. In comparison, the carbides generally paly a dominant strengthener for improving the mechanical properties of H/MEAs [13]. Moravcik et al. [15] reported in a C-doping CoCrNi MEA that the introduction of $M_{23}C_6$ carbides enabled the yield strength increasing from 335 MPa to 595 MPa, while maintaining the excellent plasticity of 62%. In addition to the strengthening effect, it was interestingly shown that the carbides can also play a constructor for the grain architecture [16]. Specifically, during annealing duration, the rapid precipitation of carbides at grain boundaries is generally in conjunction with the recrystallization; the carbides could promote recrystallization by providing favorite nucleation sites at initial annealing stage; however, the uniform extension of grain boundaries at later annealing stage is inhibited because of the Zenner pinning effects induced by carbides. This generally contributes to a refine-grained or hetero-grained microstructure in annealed alloys [12,16], that could avoid the possible loss of strength due to grain coarsening.

Inspired by the above studies, we designed a $(CoCrNi)_{93.5}Al_3Ti_3C_{0.5}$ MEA for employing the composite precipitation-strengthening strategy of $L1_2$ phase and carbides to enhance the strength-ductility synergy. In order to avoid the severe coarsening of precipitates caused by strong driving force of solid-state phase transition, a coupled process of hot-rolling and short/medium-time annealing was adopted to construct the microstructure. The interaction behaviors of multiple precipitations and their effect on grain structure evolution were focused on in this work. Besides, the deformation mechanisms of the present alloys were also revealed to get insight into the connection between microstructure and mechanical properties.

2. Materials and Methods

The investigated MEA with a nominal composition of $(CoCrNi)_{93.5}Al_3Ti_3C_{0.5}$ (at.%) was prepared by vacuum induction melting with pure elements (>99.9 purity). After drop-casting, the ingot was homogenized at 1200 °C for 4 h and then hot-rolled at 1100 °C by ~95% reduction in thickness. Subsequently, the as-rolled sheet was isothermally annealed at 950 °C for 3 min and 30 min, respectively. Any of the thermomechanical treatments were conducted in air and finished by water-quenching. For convenience, the annealed samples were code-named as HA-3 and HA-30, respectively.

Quasi-static tensile tests were performed on a universal electronic tensile testing machine (AG-X PLUS) at room temperature. The dog-bone specimens were fabricated with a gauge length of 25 mm and across-section area of 6 × 3 mm2. Tensile loading was parallel to the rolling direction with a strain rate of 1×10–3 s–1. At least three repeated tests were conducted for authenticity. An X-ray diffractometer (XRD, SmartLab-3 KW) was employed for phase identification, with an operating range from 20 to 90 deg. Microstructural observations were conducted by a SIGMA500 field-emission scanning electron microscope (SEM) equipped with Oxford Nordlys Max3 for electron backscattered diffraction (EBSD), and a Tecnai G2 F30 S-TWIN transmission electron microscope (TEM) equipped with energy-dispersive X-ray spectroscopes (EDS). The EBSD examination was performed with a step size of 0.05 μm. Both the SEM and EBSD specimens were taken along the rolled direction. After mechanically grounding and polishing, the specimens were electro-polished (15 V, 273 K) with an electrolyte composed of 90% ethanol and 10% perchloric acid (vol.%). The specimens for TEM

 doi:10.20944/preprints202408.1207.v1

analysis were mechanically thinned to ~50 μm and punched into 3 mm diameter foils, followed by ion-beam thinning at ambient temperature.

3. Results and Discussion

3.1. Phase Composition and Grain Structure

The XRD patterns of the studied samples are shown in Figure 1a. Only the typical diffraction peaks representative of FCC matrix can be detected. Of note that the peaks of the HA-30 sample shows a little asymmetry, generally indicating the presence of ordered $L1_2$ phase [17]. Through deconvolving the (111) diffraction peak (Figure 1b), the lattice constants of FCC and $L1_2$ phases were calculated to be 0.3582 nm and 0.3578 nm, respectively. Such the phenomenon of peak overlap is not obvious in the HA-3 sample (Figure 1c), so whether the presence of $L1_2$ phase needs to be further verified.

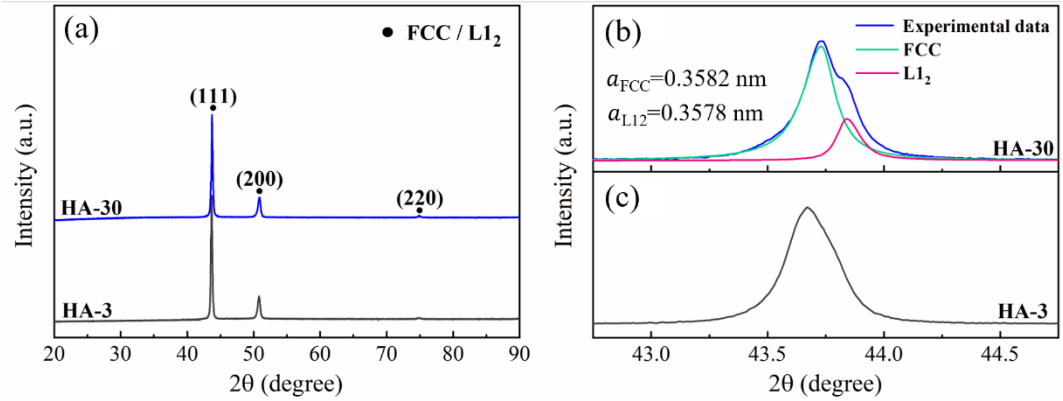

Figure 1. (a) XRD patterns of the HA-3 and HA-30 samples. Deconvolution (b) and local amplification (c) of the (111) diffraction peak for the HA-30 and HA-3 samples, respectively.

The backscatter electron (BSE) technique was employed to examine the microstructure. From the low magnification BSE images (Figure 2a, b), it is observed that the black particles are uniformly distributed in both the samples studied. Upon magnification, some fine particles distributed at grain boundaries (GBs) can be found in the HA-3 sample (Figure 2c). With the annealing time prolonging to 30 min (HA-30), the intergranular particles grew and could be clearly identified as grey and white, as shown in Figure 2d. The SEM-EDS point-scanning results (Figure 2e) reveal that the black particles are enriched in the Ti element, while the grey and white ones are enriched in the Cr and the Ni, Al, Ti elements, respectively.

In order to identify the precipitates accurately, detailed microstructure analyses of the HA-30 sample based on TEM technology were carried out. The bright-field (BF) image in Figure 3a shows a micron-sized particle, which can be identified as MC carbide by selected-area electron diffraction (SAED). The corresponding TEM-EDS mapping (Figure 3b) reveals that the MC carbide is rich in Ti, and depleted in Co, Cr, Ni, and Al, consistent with the black particles in BSE images. As reported that the higher affinity and negative mixing enthalpies of C-Ti atom pairs is favorable for the formation of MC carbides [18]. According to the calculated phase diagram in our previous study [7], it is speculated that the MC carbides were mainly inherited from the solidification phase and grow further during the solid solution and hot rolling stages, thus reaching the sizes of micrometer-scale.

 doi:10.20944/preprints202408.1207.v1

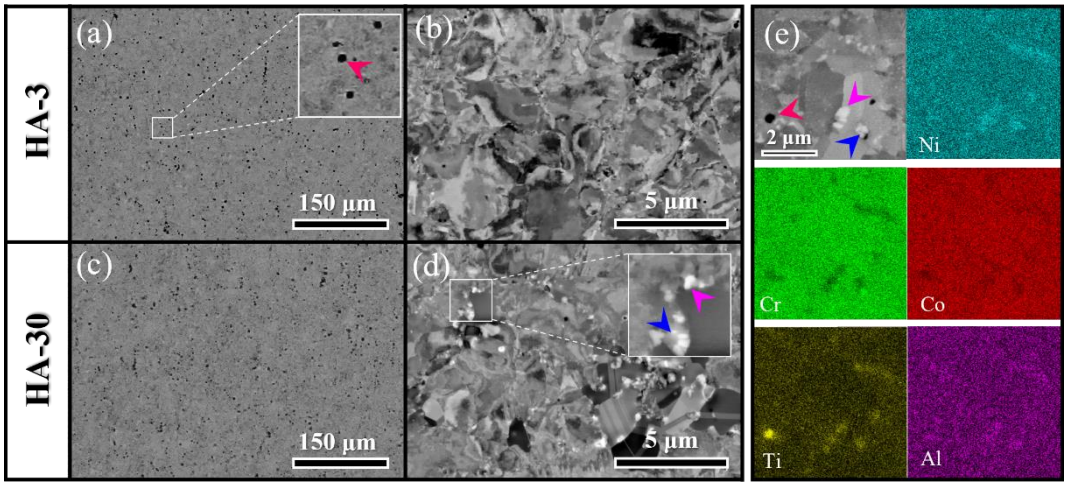

Figure 2. BSE images showing the microstructures of (a, b) HA-3 and (c, d) HA-30 samples. (e) Elemental distributions of the precipitates present in the alloy studied.

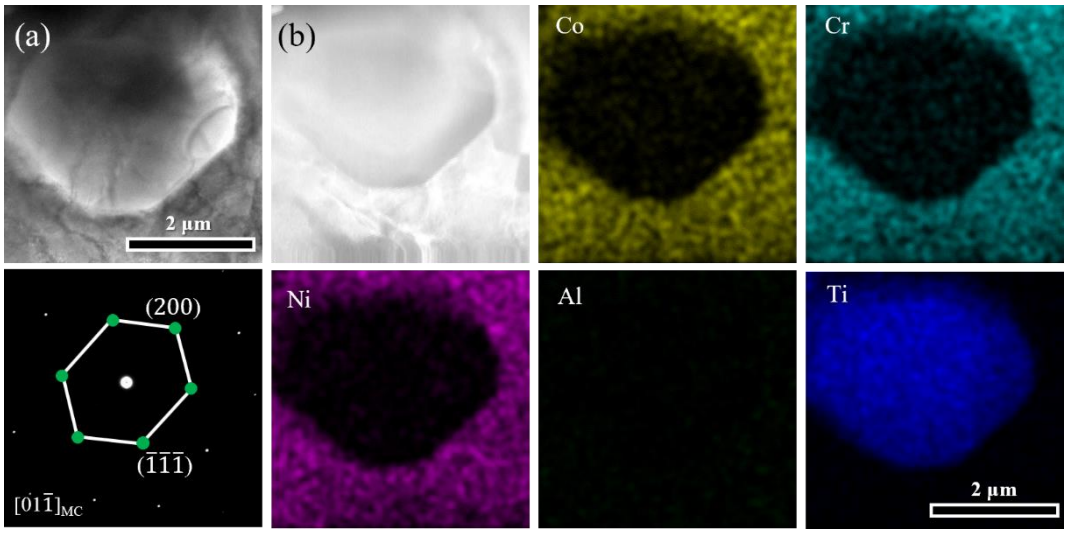

Figure 3. (a) The BF image showing the MC carbide confirmed by the corresponding SAED pattern. (b) Elemental distribution of the MC carbide.

Figure 4a shows a cluster of particles distributed at GB regions. Through combining the SAED (Figure 4b$_1$ and b$_2$) and TEM-EDS mapping (Figure 4c), two types of precipitates of $M_{23}C_6$ carbide and $L1_2$ phase were identified. The former is enriched in Cr, while the latter in Ni, Al, Ti, which is consistent with the grey and white particles in the BSE images, respectively. Upon inspection of many BSE and BF-TEM images, it is noted that the $M_{23}C_6$ carbide and $L1_2$ phase were almost always distributed adjacently. Moreover, we found that the $M_{23}C_6$ carbide, FCC matrix, and $L1_2$ phase show a cubic-cubic orientation relationship, i.e., $[110]_{M23C6}\|[110]_{FCC}\|[110]_{L12}$ (Figure 4b$_3$). These may indicate an interactive correlation between the formation of the $M_{23}C_6$ carbide and $L1_2$ phase. Specifically, the rapid diffusion of C atoms at high temperatures favors the preferential precipitation of $M_{23}C_6$ carbides at GB regions; this can not only deplete Cr to create in turn a favorable elemental environment locally enriched in Ni, Al, and Ti, but also provide favorable nucleation sites, thus contributing to the precipitation of $L1_2$ phase adjacent to the $M_{23}C_6$ carbides.

Previous reports [19,20] have shown that in the similar Al/Ti-doping 3d transition H/MEAs, the nano-scaled $L1_2$ particles are typically precipitated in the grain interior uniformly upon medium-temperature annealing. Therefore, we conducted a further observation for the intragranular microstructure of both the samples studied. Figure 5a is a BF image of the HA-30 sample, showing the residual dislocations. The SAED pattern shows the weak spots in addition to the main diffraction

 doi:10.20944/preprints202408.1207.v1

spots representative of the FCC matrix, indicative of the presence of ordered $L1_2$ phase. The dark-field (DF) image in Figure 5b shows the diffuse distribution of nano-scaled $L1_2$ particles. Figure 5c is the high-resolution (HR) TEM image and corresponding Fast Fourier transform (FFT) images. By measuring the crystal plane spacing directly, the lattice constants of FCC and $L1_2$ phases were calculated to be 0.3581 nm and 0.3577 nm, respectively, almost in agreement with that from the XRD result. Inserting the values into the equation of $\delta = 2(a_{L1_2} - a_{FCC})/(a_{L1_2} + a_{FCC})$ yielded the lattice mismatch value (δ) of 0.11%. Such the lower lattice mismatch contributed to a lower elastic-misfit energy barrier for high-density nucleation [21]. Meanwhile, the sluggish diffusion rates of solutes in multicomponent matrix and the lower interfacial energy (coherent interfaces of FCC/$L1_2$ phases) suppressed the kinetic and thermodynamic driving forces of Ostwald ripening, respectively [22,23]. These were jointly responsible for the high-density yet nanoscale of the intragranular $L1_2$ precipitates. In contrast to the HA-30 sample, almost none of the intragranular $L1_2$ precipitates were detected in the HA-3 sample, probably due to the very short annealing duration. This rationalizes the phenomenon of insignificant peak overlap in the XRD pattern of this sample.

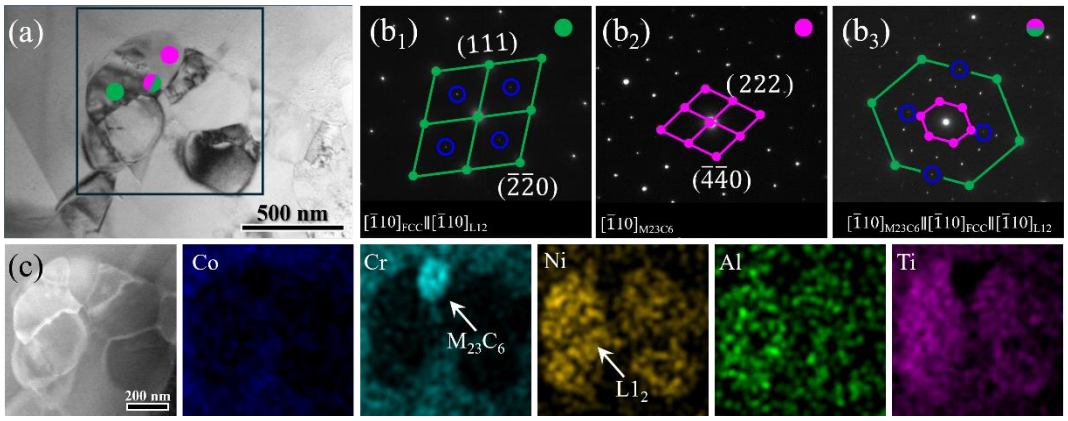

Figure 4. (a) The BF image showing a cluster of precipitates, which were identified as $M_{23}C_6$ carbides and $L1_2$ phase, respectively, by the corresponding SAED patterns (b). (c) Elemental distributions of the $M_{23}C_6$ carbides and $L1_2$ phase.

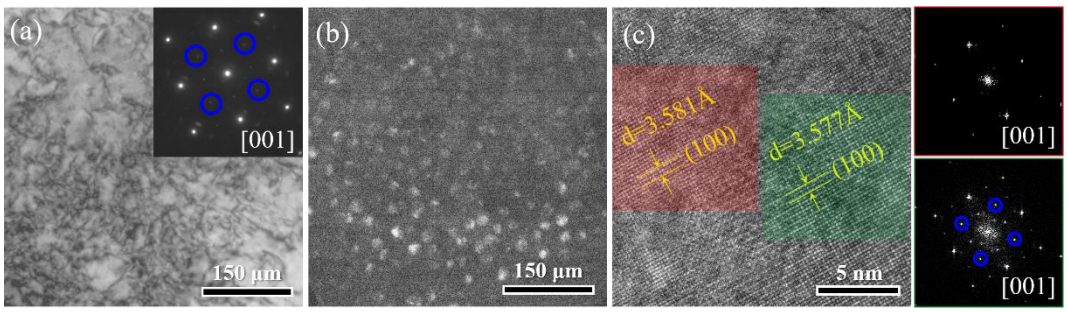

Figure 5. The TEM observations showing the intragranular $L1_2$ precipitates of the HA-30 sample. (a) BF and SAED images. (b) DF pattern. (c) HRTEM and corresponding FFT images.

EBSD examinations were conducted to uncover the recrystallization microstructure. As shown in Figure 6a and c, the inverse pole figure (IPF) maps of the present samples both show the {111} texture orientation, corresponding to the orientation peak amplitude of (111) plane in XRD patterns. The HA-3 sample presented a relatively homogenous grain structure consisting of uniformly sized equiaxed-grains (Figure 6a). Corresponding kernel average misorientation (KAM) distribution mapping (Figure 6b) shows a high density of residual dislocations almost throughout the microstructure, indicative of the lower degree of recrystallisation. As the annealing time increased to 30 min, the density of residual dislocations decreased significantly, while part of the grains were coarsened and some recrystallized fine-grains formed (Figure 6c, d). Thus, the HA-30 sample presented a heterogeneous grain structure. In this regard, in addition to the possibly uneven

 doi:10.20944/preprints202408.1207.v1

distribution of deformation storage energy, the effect of intergranular precipitation behavior may be the main reason for the inhomogeneous recrystallization [16,24]. On the one hand, the particles preferentially precipitated at GB regions provide heterogeneous nucleation sites for recrystallisation. On the other hand, the intergranular precipitates produced Zener pinning forces that inhibit the homogeneous expansion of GBs.

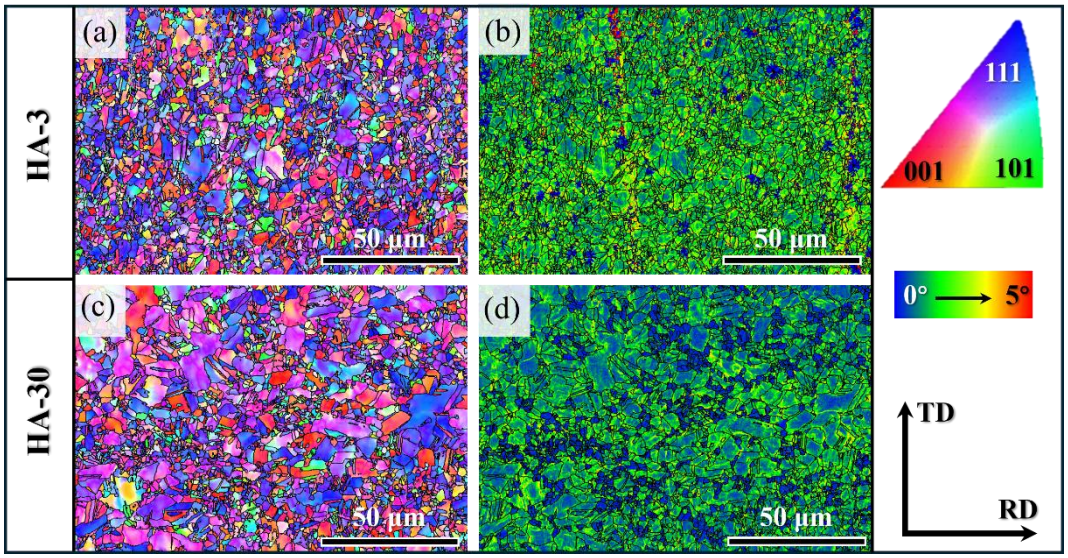

Figure 6. IPF (a, c) and KAM (b, d) images of the HA-3 and HA-30 samples, respectively. TD: transverse direction; RD: rolling direction.

3.2. Mechanical Properties

The engineering stress-strain curves of the present samples are shown in Figure 7a. The HA-3 sample exhibited yield strength (YS) of 1152 MPa, ultimate tensile strength (UTS) of 1324 MPa, and total elongation (TE) of 30%. In comparison, the YS and UTS of the HA-30 sample decreased to 937 MPa and 1202 MPa, respectively, while the TE increased to 38%. It can be inferred that the decreased YS was attributed to the decrease in dislocation density, increase in grain sizes and coarsening of intergranular precipitates. However, the additional precipitate strengthening from the intragranular $L1_2$ particles and the hetero-deformation induced (HDI) stress strengthening made some compensation for the strength. Thus, the reduction of YS was not severe. In addition, it is noted that although the HDI effect was conducive to enhancing the work-hardening response, the local stress concentration at coarsened intergranular precipitates may be a source leading to premature crack initiation (as shown in the insert in Figure 7a). Therefore, the increase of TF was not significant. Figure 7b shows the exceptional strength-ductility combination of the current samples superior to most of other similar H/MEAs [12,16,19,20,25–33], indicative of the effectiveness of the strengthening-toughening strategy in this work.

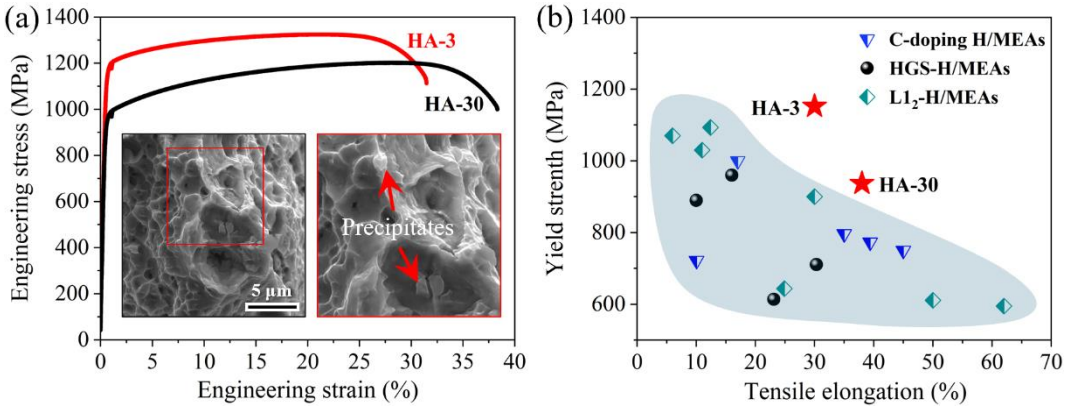

 doi:10.20944/preprints202408.1207.v1

Figure 7. (a) Engineering stress-strain curves of the studied alloy and the fracture morphology of the HA-30 sample. (b) Comparison of strength-ductility between the studied samples with the other similar H/MEAs [12,16,19,20,25–33].

3.3. Deformation Mechanisms

The engineering stress-strain curves of the present samples Detailed deformation substructures were examined via TEM analyses of the fractured samples to reveal the deformation mechanisms. As shown in Figure 8a, the typical (111) plane slip trace and the high-density dislocation walls (HDDWs) can be observed in the HA-3 sample. This generally indicates the planar slip mechanism, prevailed in FCC alloys with lower stacking fault energy (SFE) [10]. Figure 8b shows the dislocation tangles in a BF image, where the inserted SAED pattern presents the streaky lines. The deformation-induced stacking faults (SFs) are clearly shown in the corresponding DF image, as marked in Figure 8c. Figure 8d and e show the deformation twins (DTs) in the BF and DF images, respectively. The twin-related spots were marked in the corresponding SAED pattern (as shown in the insert in Figure 8d) taken along the [110] zone axis. The HRTEM image shows the Lomer-Cottrell (L-C) lock that formed by the interactions of SFs and twin boundaries (TBs), as marked in Figure 8f. The corresponding FFT image shown in the insert presents both the streaky lines and twin-related spots.

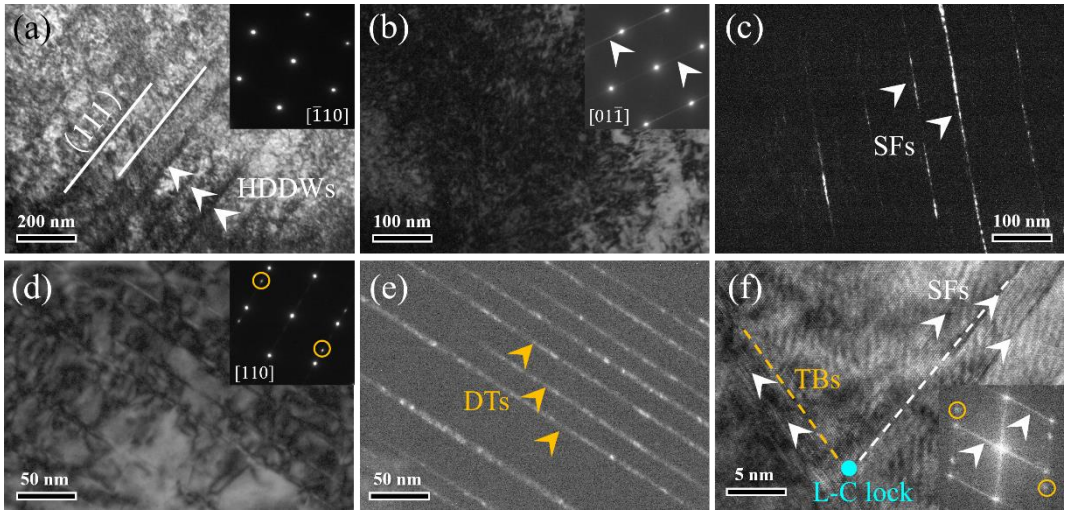

Figure 8. TEM observations of the deformed substructures of the HA-3 sample. (a) The BF image showing the (111) slip plane and HDDWs. (b, c) The SFs shown in the BF and DF images, respectively. (d, e) The DTs shown in the BF and DF images, respectively. (f) The HRTEM image showing the L-C lock formed by the interaction of SFs and TBs.

Similar to the HA-3 sample, the parallel plane slip trace and HDDWs substructures were also observed in the HA-30 sample (Figure 9a). A detailed examination of the slip region revealed almost non-existent dislocation pile-up or dislocation loop substructures, although the inserted SAED pattern indicated the presence of $L1_2$ precipitates (Figure 9b). From the DF image (Figure 9c), it seems to observe that there were new interfaces produced in the $L1_2$ precipitates after deformation making their shapes irregular. Previous reports [11,25,26] have shown that the slip dislocations are usually shearing rather than bypassing the coherent $L1_2$ precipitates because of the coherent phase interfaces with lower lattice misfit. This is effective in avoiding dislocation accumulation and thus the local stress concentrations. Figure 9d and e show the SFs in the BF and DF images, respectively. The SFs were further characterized through the HRTEM technology as shown in Figure 9f. The inserted FFT pattern taken from the marked region presents both the streaky lines and faint superlattice reflection spots. This indicates that the SFs can also shear the $L1_2$ precipitates. Noticeably, in contrast to the HA-3 sample, none of the DTs were detected upon the detailed SAED examinations for the HA-30 sample.

 doi:10.20944/preprints202408.1207.v1

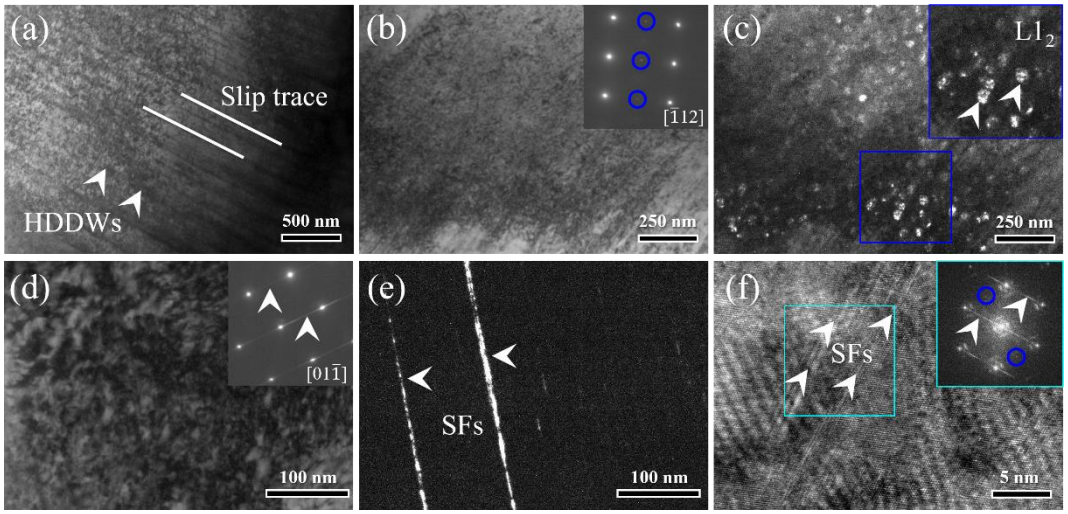

Figure 9. TEM observations of the deformed substructures of the HA-30 sample. (a) The BF image showing the parallel slip plane and HDDWs. (b, c) The $L1_2$ precipitates after deformation shown in the BF and DF images, respectively. (d, e) The SFs shown in the BF and DF images, respectively. (f) The SFs shown in the HRTEM image, and the coexistence of streaky lines and weak spots shown in the inserted FFT pattern.

Based on the above observations, it is revealed that the deformation of both the HA-3 and HA-30 samples is mainly dominated by the plane slip mechanism. One major difference is that the SFs and DTs play a mediated role in the former, while only the SFs in the latter. Previous reports [4] have shown that the lower SFE can facilitate the full dislocations to tend to plane slip or dissociate into two Shockley partial dislocations, reducing the propensity of cross slip. Referring to other studies [10,11], the SFEs of equiatomic CoCrNi-base MEAs have generally been evaluated as 20~30 mJ/m^2. It is predicted that the present $(CoCrNi)_{93.5}Al_3Ti_3C_{0.5}$ MEA in this work has also a lower SFE, contributing to the plane slip mechanism. In addition, it has been shown that the solute of C element can also promote the plane slip mechanism, as the enhanced lattice friction results in the dislocation movement slowing down [12]. For the HA-30 sample, there was an additional factor, i.e., the high density of intergranular $L1_2$ precipitates inducing the slip plane softening, contributing to the plane slip mechanism [34]. Specifically, the $L1_2$ precipitates acting as obstacles to dislocation slip that is energetically favorable for the formation of dislocation pairs [35]. As the first dislocation shears through the $L1_2$ ordered domain, that will produce high-energy bonds triggering the increased system energy; with the entry of the second dislocation with a same Burgers vector to the first one, the bonding within the ordered region will be restored and thus the system energy reduced, so it is energetically favorable [36]. After several of dislocation pairs shear through the $L1_2$ ordered domain, the resistance to dislocation movement will be reduced, and the subsequent shearing will not need the slip of dislocation pairs. As a result, the slip planes will be softened and thus promoting the plane slip mechanism.

Another point worth noting is that the absence of DTs in the HA-30 sample is also related to the intergranular $L1_2$ precipitates. It is established that the formation of DTs is closely associated with the SFs extension behavior. Previous studies [37] reported that with the SFs shearing the ordered $L1_2$ precipitates, the complex SFs (CSFs) with higher energy will be produced in their wake. Eliminating the CSFs to form twins requires the diffusion-mediated reordering within the $L1_2$ ordered domain, as revealed in the Ni-base superalloys [38]. However, this was apparently almost impossible to achieve at room temperature, and thus the formation of DTs was inhibited. In addition, it has been shown that the high density of $L1_2$ precipitates narrowing the matrix channels and thus enhancing the critical twinning stress (τ_{tw}) is also an important factor in suppressing the twinning behavior. The corresponding theorical equation as expressed below [10,36]:

 doi:10.20944/preprints202408.1207.v1

$$\tau_{tw} = \frac{2\alpha G b_p}{L} + \frac{\gamma_{ISFE}}{b_p} + \tau_{fr} \quad (1)$$

$$L = \sqrt{\frac{8}{3\pi f}} d - d \quad (2)$$

Where α is constant reflecting the dislocation character (0.5 [36]), G is the shear modulus (88.7 GPa [37]), $b_p = \frac{a}{\sqrt{6}} = 0.146$ nm (measured from the XRD result) is the Burgers vector of Shockley partial dislocations, γ_{ISFE} is the stacking fault energy (~22 mJ/m^2 [10], taken from the value of CoCrNi MEA for simplicity), τ_{fr} is the lattice friction stress (51 MPa [37]), L is the effective length of a twinning source, $f = 8\%$ and $d = 11$ nm represent the volume fraction and average diameter of the intragranular $L1_2$ precipitates (measured on average from multiple DF-TEM images). The critical shear stress and normal stress for twinning in the HA-30 sample were calculated to be 724 MPa and 2413 MPa, respectively. The latter is far higher than the sample's UTS (1070 MPa), which can rationalize the absence of DTs upon deformation to fracture.

4. Conclusions

Two strong yet ductile MEAs with a composition of $(CoCrNi)_{93.5}Al_3Ti_3C_{0.5}$ were produced by short/medium-time annealing after hot-rolling in this work. The microstructural evolution during annealing, and the deformation mechanisms upon tensile loading were revealed. The main conclusions were summarized as follows:

1. Exceptional strength-ductility combinations were both shown in the HA-3 and HA-30 samples, with the yield strength of 1152 MPa and 937 MPa, ultimate tensile strength of 1324 MPa and 1202 MPa, and total elongation of 30% and 38%, respectively.
2. Three kinds of intergranular precipitates including MC, $M_{23}C_6$ carbides, and $L1_2$ phase were detected in both the HA-3 and HA-30 samples. Note that the latter two are always distributed adjacently. It is attributed to that the preferentially formed $M_{23}C_6$ carbides provided favorable nucleation sites and complementary elemental environment for $L1_2$ precipitation.
3. The deformation of the HA-3 and HA-30 samples were both dominated by the plane slip mechanism, with the former being mediated by SFs and DTs, while the latter by SFs only. The absence of DTs in the HA-30 sample was related to the high-density of intragranular $L1_2$ precipitates which were absent in the HA-3 sample.

Author Contributions: Conceptualization, Y.C. and D.L.; Methodology, Z.Y. and S.B.; Investigation, R.X. and J.S.; Data curation, J.Z., S.L., and J.Z.; Writing—original draft preparation, Y.C.; Writing—review and editing, D.L., S.B.; Supervision, D.L. and Z.Y. All authors have read and agreed to the published version of the manuscript.

Funding: This research was funded by the National Natural Science Foundation of China (Nos. 52375392, 52071300, 52205402), and the Fundamental Research Program of Shanxi Province (CN) (No. 202203021212318).

Institutional Review Board Statement: Not applicable.

Informed Consent Statement: Not applicable.

Data Availability Statement: Data will be made available upon request.

Conflicts of Interest: The authors declare that they have no known competing financial interests or personal relationships that could have appeared to influence the work reported in this paper.

References

1. Yeh J.W.; Chen S.K., Lin S.J., Gan J.Y., Chin T.S., Shun T.T., Tsau C.H., Chang S.Y. Nanostructured high-entropy alloys with multiple principal elements: novel alloy design concepts and outcomes. *Adv. Eng. Mater*. **2004**, 6, 299–303.
2. Cantor B., Chang I.T.H., Knight P., Vincent A.J.B. Microstructural development in equiatomic multicomponent alloys. *Mater. Sci. Eng. A*. **2004**, 375–377, 213–218.

 doi:10.20944/preprints202408.1207.v1

3. Rackwitz J., Yu Q., Yang Y., Laplanche G., George E.P., Minor A.M., Ritchie R.O. Effects of cryogenic temperature and grain size on fatigue-crack propagation in the medium-entropy CrCoNi alloy. *Acta Mater.* **2020**, 200, 351–365.
4. Laplanche G., Kostka A., Reinhart C., Hunfeld J., Eggeler G., George E.P. Reasons for the superior mechanical properties of medium-entropy CrCoNi compared to high-entropy CrMnFeCoNi. *Acta Mater.* **2017**, 128, 292–303.
5. Gludovatz B., Hohenwarter A., Thurston K.V., Bei H., Wu Z., George E.P., Ritchie R.O. Exceptional damage-tolerance of a medium-entropy alloy CrCoNi at cryogenic temperatures. *Nat. Commun.* **2016**, 7, 10602.
6. Gludovatz B., Hohenwarter A., Catoor D., Chang E.H., George E.P., Ritchie R.O. A fracture-resistant high-entropy alloy for cryogenic applications. *Science* **2014**, 345, 1153–1158.
7. Chen Y.A., Li D.Z., Xie R.F., Lu H.T. Dual precipitates and heterogeneous fine-grain structure induced strength-ductility synergy in a CoCrNi-based medium-entropy alloy. *Mat. Sci. Eng. A.* **2023**, 867, 144504.
8. Gwalani B., Dasari S., Sharma A., Soni V., Shukla S., Jagetia A., Agrawal P., Mishra R.S., Banerjee R. High density of strong yet deformable intermetallic nanorods leads to an excellent room temperature strength-ductility combination in a high entropy alloy. *Acta Mater.* **2021**, 219, 117234.
9. Schuh B., Mendez-Martin F., Völker B., George E.P., Clemens H., Pippan R., Hohenwarter A. Mechanical properties, microstructure and thermal stability of a nanocrystalline CoCrFeMnNi high-entropy alloy after severe plastic deformation. *Acta Mater.* **2015**, 96, 258–268.
10. Zhao Y.L., Yang T., Tong Y., Wang J., Luan J.H., Jiao Z.B., Chen D., Yang Y., Hu A., Liu C.T., Kai J.J. Heterogeneous precipitation behavior and stacking-fault-mediated deformation in a CoCrNi-based medium-entropy alloy. *Acta Mater.* **2017**, 138, 72–82.
11. Wang J.Y., Zou J.P., Yang H.L., Dong X.X., Cao P., Liao X.Z., Liu Z.L., Ji S.X. Ultrastrong and ductile $(CoCrNi)_{94}Ti_3Al_3$ medium-entropy alloys via introducing multi-scale heterogeneous structures. *J. Mater. Sci. Technol.* **2023**, 135, 241–249.
12. Li Z.M. Interstitial equiatomic CoCrFeMnNi high-entropy alloys: carbon content, microstructure, and compositional homogeneity effects on deformation behavior. *Acta Mater.* **2019**, 164, 400–412.
13. Guo L., Ou X.Q., Ni S., Liu Y., Song M. Effects of carbon on the microstructures and mechanical properties of FeCoCrNiMn high entropy alloys. *Mat. Sci. Eng. A.* **2019**, 746, 356–362.
14. Wang Z.W., Baker I., Cai Z.H., Chen S., Poplawsky J.D., Guo W. The effect of interstitial carbon on the mechanical properties and dislocation substructure evolution in $Fe_{40.4}Ni_{11.3}Mn_{34.8}Al_{7.5}Cr_6$ high entropy alloys. *Acta Mater.* **2016**, 120, 228–239.
15. Moravcik I., Hornik V., Min´arik P., Li L.L., Dlouhy I., Janovska M., Raabe D., Li Z.M. Interstitial doping enhances the strength-ductility synergy in a CoCrNi medium entropy alloy. *Mater. Sci. Eng. A.* **2020**, 781, 139242.
16. Hu G.W., Zeng L.C., Du H., Wang Q., Fan Z.T., Liu X.W. Combined effects of solute drag and Zener pinning on grain growth of a NiCoCr medium-entropy alloy. *Intermetallics* **2021**, 136, 107271.
17. Zhang Z.H., Jiang P., Yuan F.P., Wu X.L. Enhanced tensile properties by heterogeneous grain structures and coherent precipitates in a CoCrNi-based medium entropy alloy. *Mater. Sci. Eng. A.* **2022**, 832, 142440.
18. Takeuchi A., Inoue A. Classification of bulk metallic glasses by atomic size difference, heat of mixing and period of constituent elements and its application to characterization of the main alloying element. *Mater. Trans.* **2005**, 46, 2817–2829.
19. Liu L.Y., Zhang Y., Li J.P., Fan M.Y., Wang X.Y., Wu G.C., Yang Z.B., Luan J.H., Jiao Z.B., Liu C.T., Liaw P.K., Zhang Z.W. Enhanced strength-ductility synergy via novel bifunctional nano-precipitates in a high-entropy alloy. *Int. J. Plast.* **2022**, 153, 103235.
20. Yang T., Zhao Y.L., Luan J.H., Han B., Wei J., Kai J.J., Liu C.T. Nanoparticles-strengthened high-entropy alloys for cryogenic applications showing an exceptional strength-ductility synergy. *Scr. Mater.* **2019**, 164, 30–35.
21. Jiang S.H., Wang H., Wu Y., Liu X.J., Chen H.H., Yao M.J., Gault B., Ponge D., Raabe D., Hirata A., Chen M.W., Wang Y.W., Lu Z.P. Ultrastrong steel via minimal lattice misfit and high-density nanoprecipitation. *Nature* **2017**, 544, 460–464.
22. Lukianova O.A., Rao Z., Kulitckii V., Li Z., Wilde G., Divinski S.V. Impact of interstitial carbon on self-diffusion in CoCrFeMnNi high entropy alloys. *Scr. Mater.* **2020**, 188, 264–268.
23. Peng H.L., Ling H., Li L.J., Zhang W.P. Ripening of $L1_2$ nanoparticles and their effects on mechanical properties of $Ni_{28}Co_{28}Fe_{21}Cr_{15}Al_4Ti_4$ high-entropy alloys. *Mater. Sci. Eng. A.* **2020**, 772, 138803.
24. Hu G.W., Zeng L.C., Du H., Liu X.W., Wu Y., Gong P., Fan Z.T., Hu Q., George E.P. Tailoring grain growth and solid solution strengthening of single-phase CrCoNi medium-entropy alloys by solute selection. *J. Mater. Sci. Technol.* **2020**, 54, 196–205.
25. An N., Sun Y., Wu Y., Tian J., Li Z., Li Q., Chen J., Hui X. High temperature strengthening via nanoscale precipitation in wrought CoCrNi-based medium-entropy alloys. *Mater. Sci. Eng. A.* **2020**, 798, 140213.

 doi:10.20944/preprints202408.1207.v1

26. He J.Y., Wang H., Huang H.L., Xu X.D., Chen M.W., Wu Y., Liu X.J., Nieh T.G., An K., Lu Z.P. A precipitation-hardened high-entropy alloy with outstanding tensile properties. *Acta Mater.* **2016**, 102, 187–196.
27. Qin S., Yang M.X., Jiang P., Wang J., Wu X.L., Zhou H., Yuan F.P. Designing structures with combined gradients of grain size and precipitation in high entropy alloys for simultaneous improvement of strength and ductility. *Acta Mater.* **2022**, 230, 117847.
28. Wu S.W., Wang G., Wang Q., Jia Y.D., Yi J., Zhai Q.J., Liu J.B., Sun B.A., Chu H.J., Shen J., Liaw P.K., Liu C.T., Zhang T.Y. Enhancement of strength-ductility trade-off in a high-entropy alloy through a heterogeneous structure. *Acta Mater.* **2019**, 165, 444–458.
29. Fu Z.Q., MacDonald B.E., Li Z.M., Jiang Z.F., Chen W.P., Zhou Y.Z., Lavernia E.J. Engineering heterostructured grains to enhance strength in a single-phase high-entropy alloy with maintained ductility. *Mater. Res. Lett.* **2018**, 11, 634–640.
30. Gao Q.Z., Jiang Y.J., Liu Z.Y., Zhang H.L., Jiang C.C., Zhang X., Li H.J. Effects of alloying elements on microstructure and mechanical properties of Co–Ni–Al–Ti superalloy. *Mater. Sci. Eng. A.* **2020**, 779, 139139.
31. Liu L.Y., Zhang Y., Ma J.M., Shang Y.X., Han J.H., Li J.P., Zhang Z.W. Transition of plastic deformation mechanisms governed by spacing of nano-precipitates in a high entropy alloy. *Scr. Mater.* **2022**, 217, 114771.
32. Kim J.G., Park J.M., Seol J.B., Choe J., Yu J.H., Yang S.S., Kim H.S. Nano-scale solute heterogeneities in the ultrastrong selectively laser melted carbon-doped CoCrFeMnNi alloy. *Mater. Sci. Eng. A.* **2020**, 773, 138726.
33. Li J.B., Gao B., Wang Y.T., Chen X.H., Xin Y.C., Tang S., Liu B., Liu Y., Song M. Microstructures and mechanical properties of nano carbides reinforced CoCrFeMnNi high entropy alloys. *J. Alloys Compd.* **2019**, 792, 170–179.
34. Gerold V., Karnthaler H.P. On the orgin of planar slip of F.C.C. alloys. *Acta Metall.* **1989**, 37, 2177–2183.
35. Zhang R., Zhao S., Ding J., Chong Y., Jia T., Ophus C., Asta M., Ritchie R.O., Minor A.M. Short-range order and its impact on the CrCoNi medium-entropy alloy. *Nature* **2020**, 581, 283–287.
36. Miao J., Slone C., Dasari S., Ghazisaeidi M., Banerjee R., George E.P., Mills M.J. Ordering effects on deformation substructures and strain hardening behavior of a CrCoNi based medium entropy alloy. *Acta Mater.* **2021**, 210, 116829.
37. Tong Y., Chen D., Han B., Wang J., Feng R., Yang T., Zhao C., Zhao Y.T., Guo W., Shimizu Y., Liu C.T., Liaw P.K., Inoue K., Nagai Y., Hu A., Kai J.J. Outstanding tensile properties of a precipitation-strengthened $FeCoNiCrTi_{0.2}$ high-entropy alloy at room and cryogenic temperatures. *Acta Mater.* **2019**, 165, 228–240.
38. Kovarik L., Unocic R.R., Li J., Sarosi P., Shen C., Wang Y., Mills M.J. Microtwinning and other shearing mechanisms at intermediate temperatures in Ni-based superalloys. *Prog. Mater. Sci.* **2009**, 54, 839–873.